

# Regression of solid polymer fuel strands in opposed-flow combustion with gaseous oxidizer

Clayton M. Geipel<sup>a,1,\*</sup>, Brian T. Bojko<sup>b</sup>, Christopher J. Pfützner<sup>a</sup>,  
Brian T. Fisher<sup>a</sup>, Ryan F. Johnson<sup>b</sup>

<sup>a</sup> Chemistry Division, Combustion and Reacting Transport Section, Code 6185, Naval Research Laboratory, Washington, DC 20375-5342, USA

<sup>b</sup> Laboratories for Computational Physics and Fluid Dynamics, Code 6041, Naval Research Laboratory, Washington, DC 20375-5342, USA

Received 6 January 2022; accepted 12 July 2022

Available online 6 September 2022

---

## Abstract

The combustion of solid fuels is a complex feedback loop, coupling the decomposition of the solid fuel into volatile gases with the gas-phase combustion which is responsible for the heat flux that drives decomposition. This study aims to explore the combustion of a solid fuel, hydroxyl-terminated polybutadiene (HTPB), with different mixtures of oxygen and nitrogen in an opposed-flow burner (OFB) configuration to better understand these coupled processes. An experimental OFB setup is described, which utilizes a nichrome wire and linear variable differential transformer (LVDT) to capture regression rate and shadowgraph imaging to measure flame thickness. Experimental measurements are compared with results from a complimentary one-dimensional opposed-flow combustion model with a pyrolyzing solid fuel boundary condition that conserves mass, species, and energy at the solid-gas interface. The oxidizer mass flux, ratio of oxygen to nitrogen, and separation distance of the fuel and oxidizer are varied to understand their influence on the combustion process and subsequently their effect on the regression rate. In numerical results, fuel regression rate increases when oxygen mole fraction or mass flux increase, or when separation distance decreases. Experimental regression rates and flame thicknesses are compared to simulated results. Though the actual values do not agree exactly, numerical and experimental results are reasonably close and present similar trends. These results demonstrate the utility of simple optical diagnostics in measuring OFB flames and provide a starting point for future opposed-flow combustion model improvements.

© 2022 The Combustion Institute. Published by Elsevier Inc. All rights reserved.

**Keywords:** Solid fuel; Opposed-flow burner; Regression rate; Flame thickness

---

## 1. Introduction

Increasing interest in alternative propulsion methods, from solid propellant rocket motors to solid-fuel hybrid rockets, ramjets, and scramjets,

---

\* Corresponding author.

E-mail address: [clayton.geipel.ctr@nrl.navy.mil](mailto:clayton.geipel.ctr@nrl.navy.mil) (C.M. Geipel).

<sup>1</sup> National Research Council Postdoctoral Associate.

has created a need to better understand the fundamental combustion processes of solid fuel with various oxidizers. Hydroxyl-terminated polybutadiene (HTPB) has been investigated as an ingredient in solid rocket motors, serving as the solid fuel binder and comprising  $\sim 15\%$  of the total mass of the propellant. Tingfa [1] used thermal gravimetric analysis (TGA) and differential scanning calorimetry (DSC) coupled with chromatography to explore the decomposition processes and species generation during HTPB pyrolysis. Chen and Brill [2] similarly used TGA and DSC, but utilized infrared (IR) spectroscopy to determine gaseous species while also attempting to include higher heating rates to replicate combustion-like heat fluxes to the fuel. Arisawa and Brill [3,4] utilized Fourier-transform infrared (FTIR) spectroscopy under combustion-like scenarios to better understand the gasification of HTPB leading to an estimate of the pyrolysis products and regression rates of HTPB at high temperatures.

The body of research on HTPB combustion has mostly been in conjunction with ammonium perchlorate (AP) as the primary oxidizer [5], however recent studies have been conducted to investigate HTPB as a solid fuel in various oxidation environments. Furthermore, the combustion of HTPB with air and in hybrid motors occurs at reduced pressures and temperatures as compared to those in solid rocket motors and requires additional investigation at these conditions. In an attempt to explore these conditions, Hedman [6] used a focused laser energy source to determine HTPB fuel characteristics and thermodynamic properties for applications in air-breathing solid-fuel ramjets. Additionally, Shark et al. [7] were interested in the combustion of solid fuels for hybrid rocket applications and developed an opposed-flow burner (OFB) experiment with various fuels and used pure oxygen as the oxidizer. This work assessed fuel candidates through measurements of the regression rate, observed flame structure, and flame temperatures.

The goal of an OFB configuration is to reduce the flow-field to one-dimensional theory, allowing the focus to be on the intricately coupled combustion and regression process with the added benefit of comparison to combustion models. Likewise, this study investigates the combustion of HTPB in an OFB configuration at various oxidizer concentrations, separation distances, and mass flux rates of the oxidizer both experimentally and numerically to elicit the differences in the physical processes and theory. Validating numerical results through comparison with experimental data is an important step towards the development of a reliable predictive model for HTPB combustion in real propulsion systems.

The remainder of this study is structured as follows. First, the experimental setup is presented with details given on the fuel strand preparation, the OFB, and flame imaging. Second, a numer-

ical model is presented with a description of a boundary condition that couples the regression rate, species concentrations, and temperature of the solid fuel surface to quasi-one dimensional flame theory. Next, comparisons of the experimental and numerical regression rates and flame thicknesses are presented for a range of oxidizer ratios, separation distances, and mass fluxes. Finally, conclusions are drawn and future work is discussed to improve the current approach.

## 2. Experimental setup

### 2.1. Fuel strand preparation

To prepare the fuel strands, HTPB resin (R-45M) was mixed with a curative (isophorone diisocyanate, 10 wt.%) and cure catalyst (triphenylbismuth, 0.2 wt.%) for ten minutes under room temperature and pressure. Gas was evacuated from the mixing chamber for another ten minutes of mixing in order to degas the resin. The fully mixed resin was poured into 16-mm-diameter cylindrical molds and cured at 65–70 °C for 72 h, at which point the resin was fully cured. Fuel strands were kept in a desiccator at 20 °C, 1 atm, and 15% relative humidity, and removed only for testing. Fuel strands were cut to lengths of approximately 25 mm for burn tests.

### 2.2. Opposed-flow burner

Fig. 1 is a diagram of the OFB used in this experiment.

An aluminum tube with a conical rim and inner diameter 16.5 mm was used as a fuel strand holder. A linear variable differential transformer (LVDT) (RDP Electrosense, DCV050A) applied

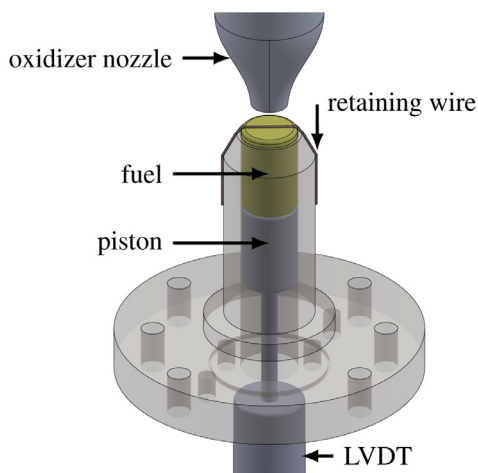


Fig. 1. OFB schematic.

a spring force to a steel piston, pressing the fuel strand into a nichrome retaining wire of diameter 0.64 mm that was attached to the fuel holder with tape. The voltage of the LVDT was measured using a digital data acquisition system (National Instruments, USB-6211). As material burned away from the fuel strand, the strand was pressed upward so that the top surface remained roughly stationary. During this process, the wire was partially submerged in a multiphase transition layer in which HTPB melted and boiled. The LVDT output voltage was used to record the fuel surface position as a function of time during the combustion process. A stainless steel oxidizer nozzle was placed in opposition to the fuel holder. The separation distance between oxidizer nozzle and fuel surface could easily be changed to investigate strain rate effects on the flame. Two mass flow controllers (Alicat, 0–250 SLPM) provided oxygen and nitrogen to the oxidizer nozzle.

Oxidizer gas was fed to a nozzle through a pipe of length 12 cm and inner diameter 1.91 cm. The oxidizer nozzle was similar to a design previously used in opposed-flow experiments [7–9]. Over a 30-mm streamwise distance, the inner diameter of the nozzle tapered from 19 mm at the inlet to 7.25 mm at the exit. The contoured shape of the nozzle was chosen to produce a top-hat exit velocity profile [10], though the exit velocity profile from this nozzle has not been measured directly.

Model rocket igniters (Estes, StarTech) were used to ignite each fuel strand. The head of the igniter rested on top of the fuel surface at the center. A relay was used to route electrical current through the igniter to initiate combustion at the desired time. Shortly afterward, a linear solenoid actuator pulled the remains of the igniter away from the flame.

A custom LabVIEW application run on Windows 10 was used to control the ignition sequence, trigger the cameras, and command mass flow controller setpoints. At preset intervals during a single burn, the mass flux and oxygen mole fraction of the oxidizer flow could be varied. By this method, data points at several different flow conditions were recorded for a single burn test. Stochastic flow controller set points showed an independence of setpoint ordering on the measured regression rate. Rarely, the retaining wire failed during a burn test. Such failures caused obvious shifts in fuel position; data collected after wire failures were discarded.

### 2.3. Flame imaging

A high-speed shadowgraph imaging system was implemented in order to measure fuel surface behavior and flame thickness in different oxidizer flows. A ground-glass diffuser was placed immediately in front of a pulsed light-emitting diode (LED) source (ISSI, LZ-620, central wavelength  $\lambda_0 = 633$  nm), and a fused silica plano-convex lens

(focal length  $f = 150$  mm, diameter  $\varnothing 50$  mm) was mounted in a lens tube, separated from the diffuser by  $f$ . This produced a roughly-collimated lightfield illuminating the burner. Images were captured through a zoom lens (Navitar, Resolv4k) using a high-speed CMOS camera (Photron, Fastcam SA5). A bandpass filter (Andover, 633FSX10-50,  $\varnothing 50$  mm,  $\lambda_0 = 633$  nm, bandwidth 10 nm) was used to admit light from the LED source and reject broadband flame luminescence.

The camera sent trigger pulses to the LED source to synchronize the camera shutter and the light pulse. Prior to burn tests, baseline lightfield images were recorded; these were later used to correct shadowgraph images for nonuniformities in the lightfield. Images of reference objects were acquired to establish image scale: 102 pixels per mm. Grayscale 12-bit shadowgraph images were acquired at 60 frames per second with exposure duration 16.4  $\mu$ s. The field of view of shadowgraph images spanned  $10 \times 10$  mm over  $1024 \times 1024$  pixels.

Two additional CMOS cameras (Mightex, SME-C050-U) fitted with zoom lenses (Navitar, MVL12M23,  $f = 12$  mm, focal ratio  $f/1.4$ ) and neutral-density filters were used to record flame luminosity during burn tests. One had an image axis perpendicular to the oxidizer nozzle axis, capturing a side view of the flame. The other obtained an inclined view, angled downward approximately  $45^\circ$  to the fuel surface. Borosilicate glass windows shielded the lenses of all three cameras from debris ejected from the burner.

### 3. Numerical model

The computational simulations utilize the counterflow diffusion flame (CDF) solver within the CANTERA software toolkit [11,12] to solve the steady-state reacting stagnation flow equations coupled with a solid-fuel boundary condition to define the fuel mass flux, pyrolysis gases, and surface temperature. The conservation of mass, species, and energy at the boundary are defined as:

$$\dot{m}_F'' = \rho_F \dot{z} = \rho_g u_g = \dot{m}_T'' \quad (1a)$$

$$\dot{m}_F'' = \dot{m}_T'' Y_F - \rho_g D_F \left. \frac{\partial Y_F}{\partial z} \right|_s \quad (1b)$$

$$0 = \dot{m}_T'' Y_{i,g} - \rho_g D_i \left. \frac{\partial Y_i}{\partial z} \right|_s \quad (1c)$$

$$\dot{m}_F'' L_v = -\lambda_g \left. \frac{\partial T}{\partial z} \right|_s \quad (1d)$$

where  $\dot{m}_F''$  is the mass flux of the solid fuel,  $\rho_F$  is the density of the HTPB,  $\dot{z}$  is the regression rate,  $\rho_g$  and

$u_g$  are the gaseous density and velocity normal to the fuel surface,  $\dot{m}''_F$  is the total mass flux in the gas phase,  $Y$  is mass fraction,  $D$  is mass diffusivity,  $L_v$  is the latent heat of vaporization of the solid to gas-phase products,  $\lambda_g$  is the thermal conductivity,  $T$  is the gaseous temperature, and  $z$  is the normal direction from the pyrolyzing surface. The subscript  $i$  refers to a given non-fuel species. The subscript  $s$  refers to conditions at the fuel surface. The subscript  $F$  refers to the fuel species. Eq. (1b) assumes the only fuel species is butadiene ( $C_4H_6$ ) coming from the fuel side, while all other species shown in Eq. (1c) can neither deposit onto nor be generated from the fuel and are balanced by the convective and diffusive fluxes at the surface in the gas phase only. Although butadiene is assumed to be the only gas produced from the pyrolysis of HTPB, other species (e.g., acetylene, ethylene, CO) are able to accumulate at the surface, limiting the value of fuel at the surface ( $Y_F$ ) in the range of  $0.6 \leq Y_F \leq 0.8$ . Lastly, Eq. (1d) accounts for the energy balance at the surface and assumes all of the heat at the surface is used to gasify the fuel, this assumes the heating of the solid fuel (an insulator) and radiation terms are negligible.

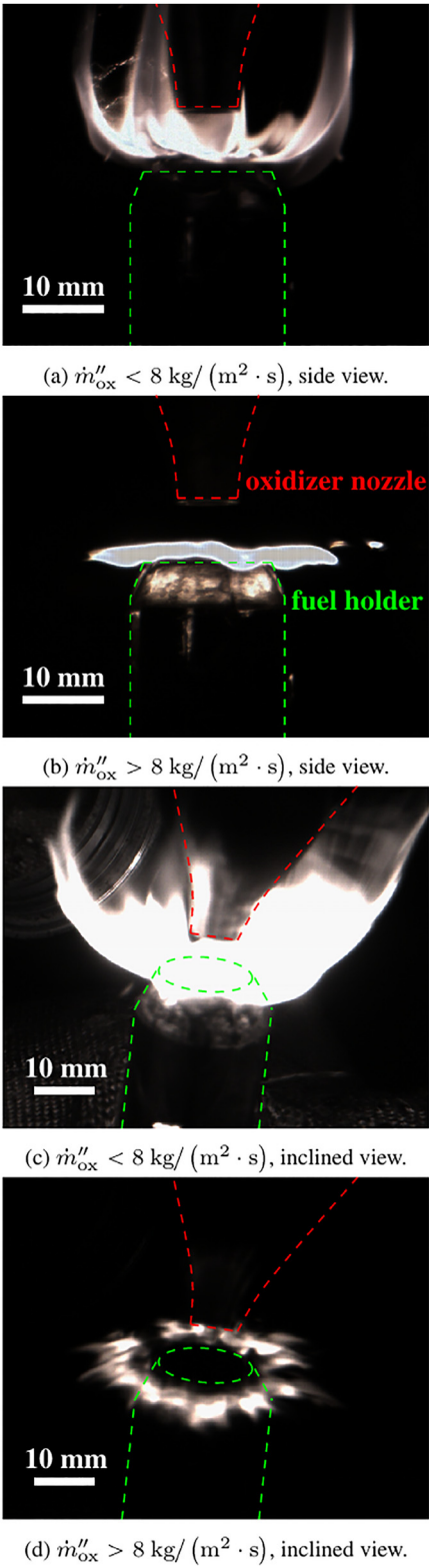
Eqs. (1a)–(1d) define an eigenvalue problem with an unknown mass flux of the fuel ( $\dot{m}''_F$ ), fuel species at the surface ( $Y_{F,s}$ ), non-fuel species at the surface ( $Y_{i,s}$ ), surface temperature ( $T_s$ ), and surface regression rate ( $\dot{z}$ ), where another equation is needed to close the system. In this case, we assume the regression rate can be modeled using an Arrhenius rate of the form  $\dot{z} = A \cdot \exp(-E_a/R_u/T_s)$ , where  $R_u$  is the universal gas constant. The pre-exponential factor ( $A_l = 3964.8$  mm/s and  $A_h = 11.04$  mm/s) and the activation energy ( $E_{al} = 13.35$  kcal/mol and  $E_{ah} = 4.91$  kcal/mol) are leveraged from the work of Evans et al. [13], where the subscripts  $l$  and  $h$  represent the low and high temperature values with  $T = 722$  K defined as the cut-off temperature.

The solid fuel boundary condition is coupled to the CDF solver in an outer loop to update the steady-state solution until the mass flux at the fuel surface converges. The detailed kinetic mechanism for high temperature 1,3-butadiene combustion developed by Laskin, Wang, and Law [14], consisting of 94 species and 614 reactions, is used in this study to define the gas-phase combustion of  $C_4H_6$ .

4. Results

4.1. Flame shape

The shape of the flame changes distinctly with oxidizer mass flux. Fig. 2 demonstrates this shape change with four Mightex CMOS images. Flames with oxidizer mass flux  $\dot{m}''_{ox} < 8$  kg/(m<sup>2</sup> s) have a curved shape caused by buoyant forces on the exhaust stream, as shown in Fig. 2(a) and (c). Flames



(a)  $\dot{m}''_{ox} < 8$  kg/(m<sup>2</sup> · s), side view.

(b)  $\dot{m}''_{ox} > 8$  kg/(m<sup>2</sup> · s), side view.

(c)  $\dot{m}''_{ox} < 8$  kg/(m<sup>2</sup> · s), inclined view.

(d)  $\dot{m}''_{ox} > 8$  kg/(m<sup>2</sup> · s), inclined view.

Fig. 2. Effects of  $\dot{m}''_{ox}$  on flame shape.

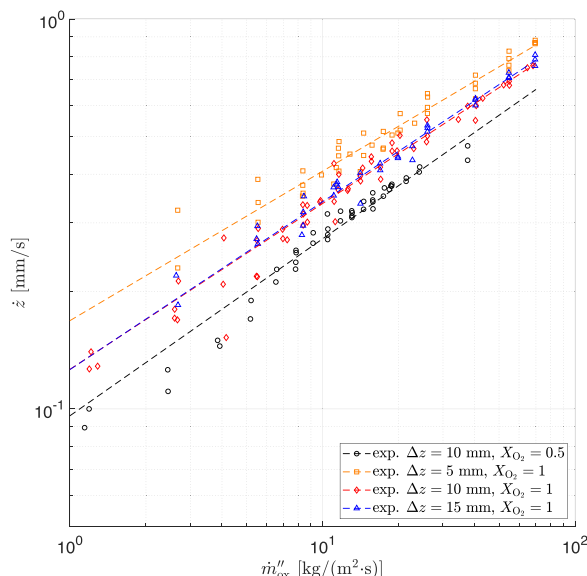


Fig. 3. Experimental (exp.) regression rates.

with  $\dot{m}''_{\text{ox}} > 8 \text{ kg}/(\text{m}^2 \text{ s})$  are flat in shape, as shown in Fig. 2(b) and (d), presumably because the momentum of the exhaust stream dominates buoyant effects. Shark et al. [7] observed a similar shape change for HTPB flames in an opposed-flow strand burner with pure oxygen oxidizer.

The mass flux at which the flame shape change occurs is approximately the same as the mass flux at which the nozzle exit flowfield transitions from laminar to turbulent. For pipe flow experiments, turbulent transition occurs for Reynolds numbers  $\text{Re}_D$  (where  $D$  is the pipe diameter) between 1700 and 3000 [15]. Assuming a top-hat velocity profile and using the nozzle exit diameter as  $D$ , a flame shape change was repetitively observed at  $\text{Re}_D \approx 2800$ . Flames with high  $\dot{m}''_{\text{ox}}$  have flame wrinkles on the order of 1 mm that are not observed in flames with low  $\dot{m}''_{\text{ox}}$ , suggesting the flame is also turbulent.

#### 4.2. Regression rate

Fig. 3 shows experimental regression rate measurements for varied oxygen mole fractions  $X_{\text{O}_2}$  and separation distances  $\Delta z$  between the fuel surface and the oxidizer nozzle exit. For each set of these varied conditions, multiple (between six and eleven) burn tests were performed over several days. For each test, regression rates were measured at multiple (between two and nine) oxidizer flow rates. The resulting 179 data points are displayed in Fig. 3. Fig. 4 shows simulated regression rates for similar conditions. Power-law fitted curves are overlaid on the data sets. The fitted curves for both experimen-

tal and simulated measurements are displayed together in Fig. 5.

The typical timing resolution for LabVIEW running on Windows 10 is 1 ms; any timing errors for individual position measurements would be random and would be averaged out in the regression rate fitting routine. The data acquisition system used has an absolute accuracy at full scale (10 V) of  $\pm 2.69 \text{ mV}$  which corresponds to an LVDT position accuracy of approximately  $\pm 13 \text{ }\mu\text{m}$ ; this uncertainty can be neglected. The LVDT used has a linearity error of  $\pm 0.32\%$ , meaning that as the LVDT shaft translates a distance  $z$ , the measured position value could be biased  $\pm 0.0032z$  and the measured regression rate value could be biased  $\pm 0.0032\dot{z}$ . The accuracy of the mass flow controllers used is within 0.8% of the measured mass flow plus 0.2% of the full scale; at the maximum flow used in this experiment, this results in a mass flux uncertainty of  $\pm 1.46 \text{ kg}/(\text{m}^2 \cdot \text{s})$ .

Simulations show three trends in regression rates as other variables are modified. Regression rate ( $\dot{z}$ ) increases when (1)  $\dot{m}''_{\text{ox}}$  increases, (2)  $X_{\text{O}_2}$  increases, or (3)  $\Delta z$  decreases. Experimental results follow the first two trends. However, in experiments, while  $\dot{z}$  increases significantly when decreasing  $\Delta z$  from 10 to 5 mm,  $\dot{z}$  is unchanged when decreasing  $\Delta z$  from 15 to 10 mm. The  $\Delta z = 5 \text{ mm}$  experimental case was unique in that the fuel surface did not remain flat throughout burn tests; the high strain rate caused the fuel surface to become somewhat concave. Shadowgraph images for this case also show droplets of liquid HTPB that were reg-

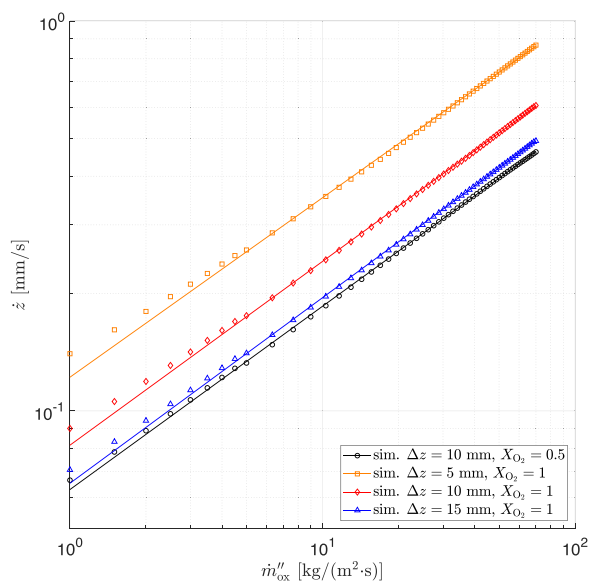


Fig. 4. Simulated (sim.) regression rates.

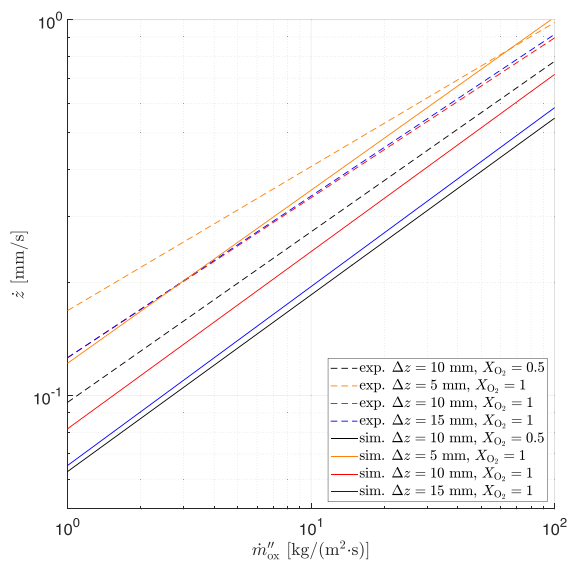


Fig. 5. Comparison of fitted curves for experimental and simulated regression rates.

ularly expelled radially from the edge of the fuel surface. Both of these factors may have increased the regression rate for this case.

Regression rate expressions [16] typically take the form

$$\hat{z} = a(\dot{m}''_{\text{ox}})^{n_1} p^{n_2} T^{n_3}. \tag{2}$$

This equation is used to determine a predicted value of regression rate  $\hat{z}$  as a function of oxidizer mass flux, oxidizer pressure  $p$  and temperature, and fitted coefficients  $a$  and  $n_i$ . This is sometimes mod-

ified to include geometric terms such as the length of the fuel grain within a combustor.

Oxidizer pressure and temperature were kept constant in this experiment (room conditions at stagnation). This permits the simplified form of the regression rate expression

$$\hat{z} = a(\dot{m}''_{\text{ox}})^n. \tag{3}$$

The fitted curves overlaid on the data points in Figs. 3–5 are of this form. These figures use logarithmic scales so that the exponential coefficient  $n$



Table 1

Power law models for experimental and simulated data sets. Uncertainties provide 95% confidence intervals.

exp. / sim.	$\Delta z$ [mm]	$X_{O_2}$	$N$	$a$ [(m <sup>3</sup> /kg) <sup>1/n</sup> ] · 10 <sup>-4</sup>	$n$	$R^2$
exp.	10	0.5	44	0.960 ± 0.089	0.454 ± 0.033	0.96
exp.	5	1	45	1.684 ± 0.142	0.383 ± 0.024	0.96
exp.	10	1	56	1.263 ± 0.089	0.425 ± 0.022	0.97
exp.	15	1	34	1.262 ± 0.092	0.430 ± 0.021	0.98
sim.	10	0.5	58	0.628 ± 0.004	0.470 ± 0.002	> 0.99
sim.	5	1	58	1.222 ± 0.002	0.460 ± 0.004	> 0.99
sim.	10	1	58	0.812 ± 0.009	0.471 ± 0.002	> 0.99
sim.	15	1	58	0.652 ± 0.006	0.476 ± 0.002	> 0.99

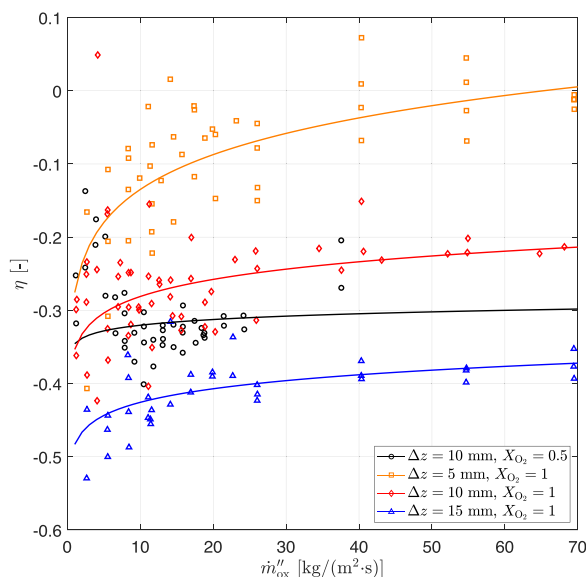


Fig. 6. Relative difference between simulation and experiment.

can be easily interpreted as the slope of a linear fit in log-log space.

Table 1 provides a summary of the various test conditions with values for  $a$ ,  $n$ , and the coefficient of determination  $R^2$  for each power law fit.  $N$  is the number of observations in each set of test conditions. All tests were limited to  $\dot{m}''_{ox} < 70$  kg/(m<sup>2</sup> s) due to oxidizer supply system constraints. Tests with  $X_{O_2} = 0.5$  were further limited to  $\dot{m}''_{ox} < 40$  kg/(m<sup>2</sup> s); increasing mass flux beyond this point caused extinction.

Fig. 6 shows the relative difference  $\eta$  between simulated and experimental regression rates for the different oxidizer cases. The symbols show the relative difference between the simulation fitted curve and each experimental data point:

$$\eta_1 = \frac{\hat{z}_{sim}(\dot{m}''_{ox}) - \dot{z}_{exp}}{\dot{z}_{exp}}, \quad (4)$$

while the curves show the relative difference between fitted regression rate expressions for simulation and experiment:

tion and experiment:

$$\eta_2(\dot{m}''_{ox}) = \frac{\hat{z}_{sim}(\dot{m}''_{ox}) - \hat{z}_{exp}(\dot{m}''_{ox})}{\hat{z}_{exp}(\dot{m}''_{ox})}. \quad (5)$$

The underprediction of experimental regression rate by the simulation is less severe at smaller values of  $\Delta z$  and larger values of  $\dot{m}''_{ox}$ . Higher-order mechanisms were applied to the model in an attempt to improve agreement with experimental data, but simulated regression rates were insensitive to the model chosen.

Shark et al. [7] performed OFB tests with 10-mm-diameter HTPB strands, an oxidizer nozzle similar to the one used in the current work,  $\Delta z = 10$  mm, and  $X_{O_2} = 1$ . They reported a change in curve fitting parameters from laminar flow ( $a = 1.57 \times 10^{-4}$  (m<sup>3</sup>/kg)<sup>1/n</sup>,  $n = 0.19$ ) to turbulent flow ( $a = 0.82 \times 10^{-4}$  (m<sup>3</sup>/kg)<sup>1/n</sup>,  $n = 0.49$ ). In the current work, no such change in the power law fit is observed at the laminar-turbulent transition. For  $\Delta z = 10$  mm and  $X_{O_2} = 1$ , the simulated

curve fitting parameters are very similar ( $a$  within 1%,  $n$  within 5%) to the parameters for the turbulent experiments in Shark et al.

4.3. Flame thickness

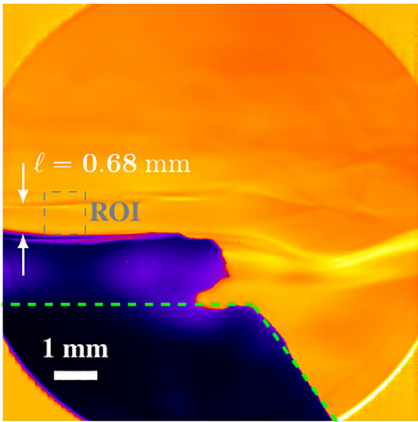
Shadowgraph images of the OFB flame show relatively-stable density gradients offset around 0.5–1 mm from the fuel surface. This is the upper boundary of a reaction zone that extends nearly to the surface of the fuel. Fig. 7 displays single acquisitions from three different test conditions with the flame thickness  $\ell$  notated. In addition to the standing density gradients, luminous patches and dark patches of soot can be seen.

Values for  $\ell$  were calculated using the following method. For each shadowgraph image, a region of interest (ROI) was selected with a width of  $W = 1$  mm in the radial direction  $r$ . The ROI was offset 1 mm from the left side of the image (which is the side closest to the center of the fuel strand). Here, the flame boundary was steadier; farther away from the center of the fuel strand, unsteady flow effects caused the flame boundary to oscillate. The ROI had a height of 1 mm in the axial  $z$ -direction, and the bottom of the ROI was placed at the fuel surface. Within the ROI, a corrected mean shadowgraph intensity  $I_c(j)$  was calculated as

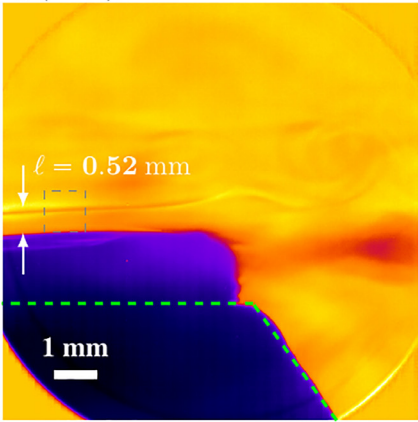
$$I_c(j) = \frac{1}{W} \sum_{i=1}^W [I(i, j) - I_0(i, j)], \tag{6}$$

where  $i$  and  $j$  are pixel indices in the  $r$  and  $z$  directions, respectively,  $I$  is the matrix of shadowgraph image pixel intensities, and  $I_0$  is the matrix of pixel intensities for a background lightfield image. For an example image, the profile of  $I_c$  as a function of  $z$  is shown in Fig. 8. The density gradients corresponding to the flame boundary appear in  $I_c(z)$  profiles as a prominent local minimum with an adjacent local maximum on one or both sides. The location of the most prominent local minimum in each  $I_c(z)$  profile is used to define the flame boundary for the corresponding shadowgraph image; the value of  $z$  of this point is taken as  $\ell$ . This process was repeated for a sequence of 50 consecutive images at each of several oxidizer flow conditions. This method could not be used to measure flame thicknesses for the  $\Delta z = 5$  mm case; the perspective of the camera and the concave fuel surface made it impossible to determine the exact position of the fuel surface. Shadowgraph images for  $\Delta z = 15$  mm produced density gradients at a height above the fuel surface that varied significantly from image to image, precluding useful comparison with other cases.

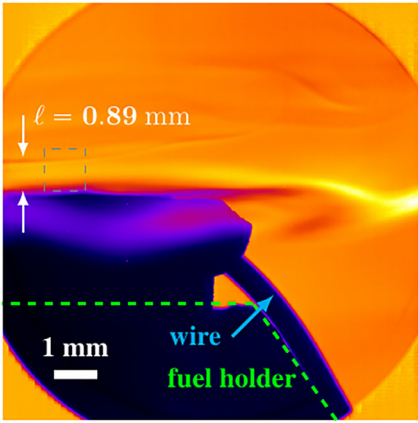
Perturbations in shadowgraph intensity are proportional to third-order spatial gradients in refractive index. Because refractive index is proportional to density, shadowgraph images reveal locations where third-order spatial gradients in density are



(a)  $X_{O_2} = 1$ ,  $\Delta z = 10$  mm,  $\dot{m}''_{ox} = 26.0$  kg/(m<sup>2</sup> · s).



(b)  $X_{O_2} = 0.5$ ,  $\Delta z = 10$  mm,  $\dot{m}''_{ox} = 24.3$  kg/(m<sup>2</sup> · s).



(c)  $X_{O_2} = 1$ ,  $\Delta z = 10$  mm,  $\dot{m}''_{ox} = 14.4$  kg/(m<sup>2</sup> · s).

Fig. 7. Shadowgraph images, background corrected, false color.



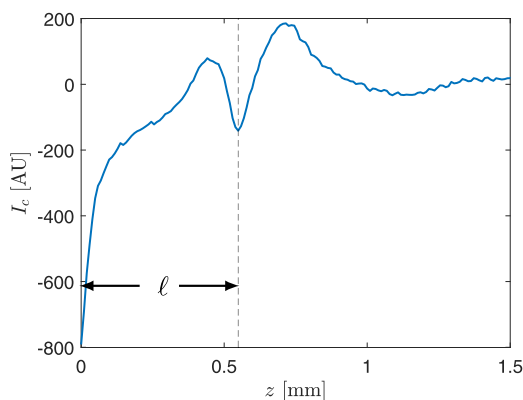


Fig. 8. Shadowgraph intensity as a function of height above the fuel surface for the image shown in Fig. 7(b).

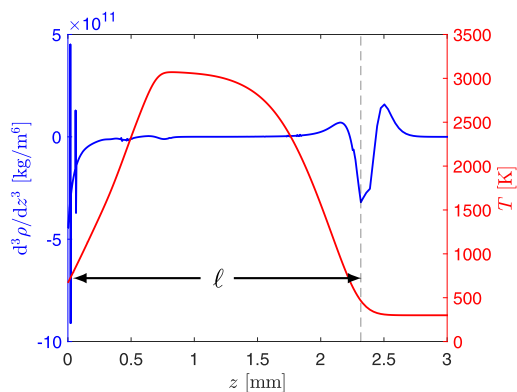


Fig. 9. Simulated shadowgraph intensity as a function of height above the fuel surface.  $X_{O_2} = 1$ ,  $\Delta z = 15$  mm,  $\dot{m}''_{ox} = 5$  kg/(m<sup>2</sup> s).

non-zero [17]. This can be represented as

$$I - I_0 \propto \frac{d^3 n}{dz^3} \propto \frac{d^3 \rho}{dz^3}, \quad (7)$$

where  $n$  is refractive index. Predicted values of  $d^3 \rho / dz^3$  were calculated from flame simulations using fourth-order Legendre polynomials.

Fig. 9 shows this quantity and temperature as functions of  $z$  for one example case. The peak temperatures for cases with  $X_{O_2} = 1$  vary from approximately 3050 to 3200 K; they are close to the  $p = 1$  atm  $C_4H_6$  adiabatic flame temperature of 3188 K. The location where local temperature falls to the temperature of the oxidizer stream is accompanied by large perturbations in  $d^3 \rho / dz^3$ . Similar to profiles of  $I_c$ , these perturbations feature a single prominent trough. The trough always has an adjacent peak on either side.  $\ell$  was defined as the distance from the fuel surface to the most prominent local minimum, disregarding extreme local fluctuations in  $d^3 \rho / dz^3$  that occur in some cases at positions very close to the fuel surface ( $z < 0.2$  mm).

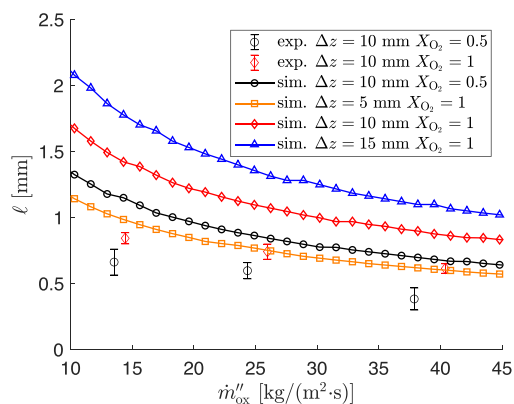


Fig. 10. Comparison between experimental and simulated flame thicknesses. Error bars are bounded at  $\pm$  one standard deviation.

Fig. 10 plots simulated values of  $\ell$  as functions of  $\dot{m}''_{ox}$  for three sets of test conditions, along with selected experimental measurements. The simulations show three trends:  $\ell$  decreases when (1)  $\dot{m}''_{ox}$  increases, (2)  $X_{O_2}$  decreases, or (3)  $\Delta z$  decreases. In experimental measurements, the first two trends are apparent, and the current image set does not allow evaluation of the third. Additionally, the simulations overpredict  $\ell$  at any given set of conditions by approximately a factor of two. This overprediction of  $\ell$  may be related to the typical underprediction of  $\dot{z}$ . If the simulated heat release is occurring too far from the fuel surface, then heat feedback to the surface is reduced, resulting in slower regression.

## 5. Conclusions

In this work, an OFB was set up experimentally and modeled numerically to investigate the combustion of HTPB at various conditions. The oxidizer mass flux, ratio of oxygen to nitrogen, and fuel-oxidizer separation distance were varied to observe their effects on the regression rates and flame thicknesses. The experimental setup utilized an LVDT to measure regression and a shadowgraph imaging system to measure the flame thickness above the fuel surface. A numerical model was presented that couples mass, species, and energy conservation equations at the solid-gas interface with the one-dimensional reacting stagnation flow equations to estimate the steady-state solution of a HTPB flame. Comparing results of the experimental and numerical regression rates showed good agreement in some of the trends: increases in  $\dot{m}''_{ox}$  or  $X_{O_2}$  result in increases in  $\dot{z}$ . However, while decreases in  $\Delta z$  resulted in increased  $\dot{z}$  in simulations, the experimental trend between these parameters was less clear. Experimental and computational flame thickness results also show trendwise agreement:  $\ell$  decreases when  $\dot{m}''_{ox}$  increases or when

$X_{O_2}$  decreases. Considering that the heat flux to the surface directly impacts the regression rate, it is unsurprising that the regression rate and flame thickness trends have an inverse correlation. The smaller  $\ell$  is, the larger  $\dot{z}$  will be, until the flame is strained beyond its limits and extinguishes. The shadowgraph and regression rate data are two independent measurements that confirm this observation.

The strong trendwise agreement observed here between experimental and numerical results is encouraging, and is a solid foundation on which to build toward a more complete and accurate model. Future work will include an improvement in the fuel decomposition boundary condition to account for potentially exothermic reactions to push the heat release closer to the surface and to relax the assumption of butadiene being the primary species evolving from the surface. If the fuel pyrolyzes into lighter hydrocarbons closer to the surface, fewer endothermic reactions in the gas phase will be necessary to convert the volatile gases to reactant products, potentially moving the flame closer to the surface. Applying higher-order mechanisms to the model demonstrated no noticeable difference in the overall regression rate than that of the 1,3-butadiene mechanism used in this study. A better description of the polymer chain decomposition at the surface will likely be beneficial to capturing important pathways critical to modeling regression rates.

In future work, optical diagnostics will also be used to more fully describe the flame, enabling better comparison with simulations, specifically relating to sensitivities of the chosen reaction mechanism. Concentration profiles of intermediate combustion species can be obtained through laser-induced fluorescence (LIF) or coherent anti-Stokes Raman spectroscopy (CARS). Gas-phase temperature measurements can be made through CARS or through thermometry of seeder particles (e.g., particle image thermometry) or seeder gases (e.g., two-photon absorption LIF). Finally, future work should also explore the phenomenon of HTPB erosion: the ejection of unburned HTPB droplets from the fuel surface in high-strain conditions. Shadowgraph images could be used to quantify the portion of regression rate attributable to combustion and the portion attributable to erosion.

### Declaration of Competing Interest

The authors declare that they have no known competing financial interests or personal relationships that could have appeared to influence the work reported in this paper.

### Acknowledgments

The authors thank the Office of Naval Research for funding this work, both directly through the En-

ergetic Materials program managed by Dr. Chad Stoltz and indirectly through the Naval Research Laboratory Base Program. C.M.G. was supported through a National Research Council postdoctoral associateship award administered by the National Academies of Science, Engineering, and Medicine. The authors also thank Drs. Matthew Finn and Albert Epshteyn for their work in preparing HTPB strands and Dr. Rohit Jacob for his contribution to the LabVIEW control application.

### References

- [1] D. Tingfa, Thermal decomposition studies of solid propellant binder HTPB, *Thermochim. Acta* 138 (2) (1989) 189–197.
- [2] J.K. Chen, T.B. Brill, Chemistry and kinetics of hydroxyl-terminated polybutadiene (HTPB) and diisocyanate-HTPB polymers during slow decomposition and combustion-like conditions, *Combust. Flame* 87 (1991) 217–232.
- [3] H. Arisawa, T.B. Brill, Flash pyrolysis of hydroxyl-terminated polybutadiene (HTPB) I: analysis and implications of the gaseous products, *Combust. Flame* 106 (1996) 144–154.
- [4] H. Arisawa, T.B. Brill, Flash pyrolysis of hydroxyl-terminated polybutadiene (HTPB) II: implications of the kinetics to combustion of organic polymers, *Combust. Flame* 106 (1996) 131–143.
- [5] C. Dennis, B. Bojko, On the combustion of heterogeneous AP/HTPB composite propellants: a review, *Fuel* 254 (2019) 115646.
- [6] T.D. Hedman, Radiation-induced pyrolysis of solid fuels for ramjet application, *Propuls. Power Res.* 5 (2) (2016) 87–96.
- [7] S.C. Shark, C.R. Zaseck, T.L. Pourpoint, S.F. Son, Solid-fuel regression rates and flame characteristics in an opposed flow burner, *J. Propuls. Power* 30 (6) (2014) 1675–1682.
- [8] G. Young, C. Roberts, S. Dunham, Combustion behavior of solid oxidizer/gaseous fuel diffusion flames, *J. Propuls. Power* 29 (2) (2013) 362–370.
- [9] G. Young, G.A. Risha, A.G. Miller, R.A. Glass, J.T.L. Connell, R.A. Yetter, Combustion of alane-based solid fuels, *Int. J. Energ. Mater. Chem. Propuls.* 9 (3) (2010) 249–266.
- [10] J.M. Bergthorson, K. Sone, T.W. Mattner, P.E. Dimotakis, D.G. Goodwin, D.I. Meiron, Impinging laminar jets at moderate Reynolds numbers and separation distances, *Phys. Rev. E* 72 (6 Pt 2) (2005) 066307.
- [11] D.G. Goodwin, R.L. Speth, H.K. Moffat, B.W. Weber, Cantera: an object-oriented software toolkit for chemical kinetics, thermodynamics, and transport processes, 2021. Available at <https://www.cantera.org>, version 2.5.1.
- [12] R.J. Kee, M.E. Coltrin, P. Glarborg, H. Zhu, *Chemically Reacting Flow: Theory, Modeling, and Simulation*, John Wiley and Sons Inc., 2017.
- [13] B. Evans, E. Boyer, K. Kuo, G. Risha, M. Chiverini, Hybrid rocket investigations at Penn State University's high pressure combustion laboratory: overview and recent results, in: 45th AIAA/ASME/SAE/ASEE Joint Propulsion Conference & Exhibit, 2009.

- [14] A. Laskin, H. Wang, C. Law, Detailed kinetic modeling of 1,3-butadiene oxidation at high temperatures, *Int. J. Chem. Kinet.* 32 (2000) 589–614.
- [15] K. Avila, D. Moxey, A. de Lozar, M. Avila, D. Barkley, B. Hof, The onset of turbulence in pipe flow, *Science* 333 (6039) (2011) 192–196.
- [16] S. Leisch, D.W. Netzer, Solid fuel ramjets, in: G.E. Jensen, D.W. Netzer (Eds.), *Tactical Missile Propulsion*, American Institute of Aeronautics and Astronautics, Reston, Virginia, 1996.
- [17] W.D. Bachalo, Methods for compressible flows, in: A.J. Smits, T.T. Lin (Eds.), *Flow Visualization: Techniques and Examples*, second ed., Imperial College Press, London, 2012, pp. 236–237.